Deep Learning-Based DenseNet-CNN Algorithmic Tool for Chest X-Ray Image Analysis: Automatic Diagnosing Diverse Lung Diseases and Abnormalities:

Baraka H.Kimwanga[1], Li Li[2]

[1](Department of Electronic Engineering, Tianjin University of Technology and Education, Tianjin, China)

Abstract:
Background*: The increase in morbidity and mortality rates has made lung diseases a significant global public health concern. The emergence of the COVID-19 pandemic in late 2019 has brought even greater urgency for early and accurate diagnosis and management of these diseases. Chest X-rays are vital in identifying and monitoring lung diseases; however, accurate interpretation is challenging, time-consuming for large datasets, and prone to human error—particularly when detecting subtle signs or early stages of the diseases.*
Materials and Methods*: This paper presents a deep-learning-based CNN algorithm that utilizes transfer learning: to develop an automated AI tool capable of independently identifying various abnormalities and detecting diverse lung diseases in Chest X-ray images. The model was trained and tested on the Chest X-ray 14 dataset containing 112,120 images from 30,805 patients across 14 categories of lung diseases—using the fine-tuned DenseNet architecture.*
Results*: The designed model achieved an average AUC-ROC score of 0.83 on the test set—surpassing previous studies. Furthermore, the model's performance evaluated on an independent dataset—from multiple sources—also demonstrated comparable results—highlighting the generalizability in new datasets.*
Conclusion: *This study indicates that the developed automated AI tool offers a promising solution to the challenges of interpreting chest X-ray images, potentially improving patient outcomes, reducing healthcare costs, and saving lives.*
Key Words*: Convolution Neural Network (CNN), Chest X-Ray (CXR), Deep-learning (DL), Densely Connected Convolutional Network (DenseNet), Lung Diseases*

I. Introduction

Lung diseases are medical conditions that affect the lungs and respiratory system. These conditions develop from various causes such as infections, genetic factors, or environmental factors like smoking, pollution, or chemical exposure. Lung diseases manifest in several types, from acute conditions like pneumonia and bronchitis to chronic conditions such as asthma, lung cancer, and COPD. These diseases often exhibit diverse symptoms, including coughing, shortness of breath, wheezing, chest pain, and fatigue [1], [2]. Consequently, lung diseases have become a substantial cause of morbidity and mortality globally, leading to millions of deaths annually—particularly in low and middle-income countries [3], [4].

The outbreak of the COVID-19 pandemic in late 2019 has emphasized the critical importance of diagnosing and managing lung conditions: not only to prevent infection in individuals with pre-existing lung diseases but also to reduce the risk of severe illness to those already infected [5], [6]. While chest X-rays are a fast, cost-effective, and non-invasive imaging tool that provides valuable and relevant information for diagnosing lung diseases, accurately interpreting the images remains challenging for subtle abnormalities or early-stage diseases. The process relies on the expertise and experience of radiologists, making it expensive, time-consuming, and prone to human errors —resulting in missed or incorrect diagnoses [7]–[10].

In recent years, Artificial Intelligence (AI) has established itself as a dominant and potent technology in medical imaging [11], [12]. By automatically and objectively analyzing images, AI can achieve improved levels of accuracy. Hence, incorporating AI into the analysis of Chest X-ray images can aid in reducing subjectivity interpretation by radiologists [13]. However, earlier studies have suggested that the top traditional machine learning AI algorithms, including support vector machines (SVMs) and decision trees, have certain drawbacks. Specifically, they are subjective due to their dependence on expert domain knowledge and manual feature engineering. Additionally, these techniques are not well-suited for handling large unstructured datasets and can be time-consuming [14], [15].

The capability of Deep learning (DL) to mimic human brain behavior in solving intricate problems—by training artificial neural networks in multiple computational layers: has exhibited immense potential in medical imaging analysis [16]–[18]. As a result, DL has emerged as breathtaking AI innovation in Chest X-ray imaging [19]. With the help of the CNN algorithm, it is now viable to effectively analyze and categorize high-dimensional Chest X-ray images [20] —as the algorithm extracts relevant patterns and structures from numerous data, regardless of their variation in qualities—without explicitly feature engineering. Hence, it computes faster and achieves accurate results at a low cost [21]–[23].

This research study showcases an AI algorithmic tool that diagnoses lung diseases and detects several lung abnormalities from a chest X-ray image—by employing deep learning Convolutional Neural Networks (CNNs) algorithm. The paper is structured as follows: Section I provides background information; Section II outlines the materials used and justifies the proposed methods; Section III presents the results obtained; Section IV interprets and analyses the study findings; and Section V concludes the paper.

II. Material And Methods

This section provides a comprehensive description of the materials and methods used. It includes the datasets (ChestX-ray14), proposed methodology (Deep-Learning Algorithm), and model design: to ensure the reproducibility and validity of our findings.
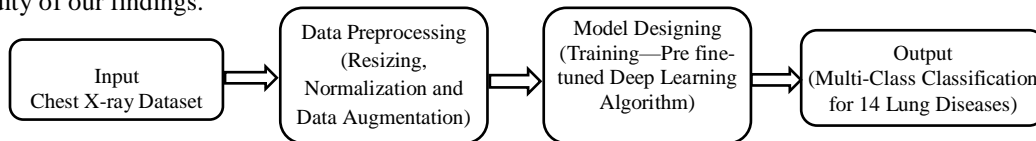

Fig 1: Block Diagram Illustrating the Flow of Model System Design

Dataset

The ChestX-ray14 database from the National Institutes of Health Clinical Center (NIH), which is publicly available and has privacy and security measures in place, was used. The dataset contains 112,120 front-view chest X-ray images with 14 different thoracic pathologies labeled by a panel of four expert radiologists. These images come from 30,805 unique patients [24].

Data Preprocessing: The datasets are labeled with 0 for absence and 1 for the presence of 14 different thoracic pathologies, including Atelectasis, Cardiomegaly, Effusion, Infiltration, Mass, Nodule, Pneumonia, Pneumothorax, Consolidation, Edema, Emphysema, Fibrosis, Pleural Thickening, and Hernia. To ensure compatibility and computational efficiency with the DenseNet architecture—trained on pre-trained ImageNet [25], [26], the images are resized into 224 x 224 pixels and normalized the values to a mean of 0 and a standard deviation of 1. The dataset is respectively split in a ratio of 80:10:10 for training, validation, and testing—while employing data augmentation techniques such as rotations, flips, and shifting: to increase data diversity [27].
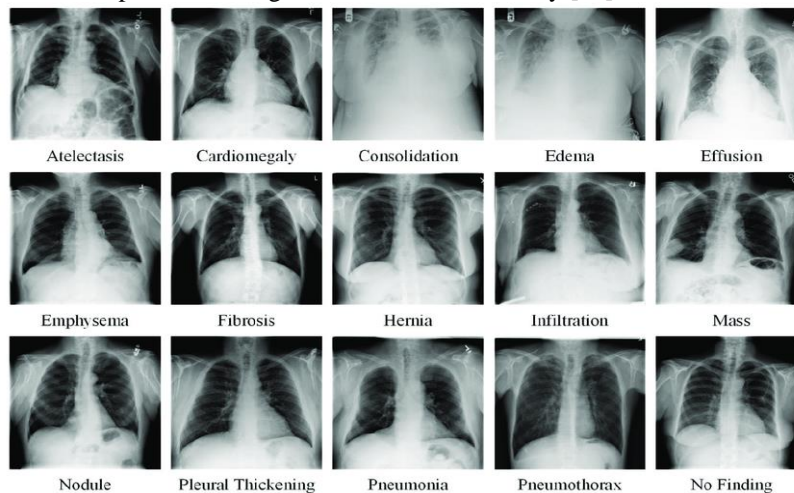

Fig 2: Chest X-ray Images Representing 14 Thoracic Pathologies

Addressing Class imbalance: The imbalanced class distribution is a significant challenge in the ChestX-ray14 dataset—where some pathologies are much rarer than others—leading to a better performance (model bias) towards the more prevalent classes like Infiltration (25%), Effusion (15%), and Atelectasis (10%) than on hernia (0.1%) and pneumonia (2%) classes. Hence, this study addresses the issue using a Transfer Learning approach via DenseNet architecture.

DenseNet 121 Architecture

The DenseNet, or Densely Connected Convolutional Network, is a robust CNN architecture that has transformed the field of medical imaging. Being trained on the ImageNet dataset, the architecture achieves a state-of-the-art performance by connecting each layer to all subsequent layers in a feed-forward manner to maintain feature maps while using fewer parameters [28]. With this attribute, DenseNet has outperformed traditional CNNs: in addressing issues such as information loss, vanishing gradients, and overfitting—whenever training large datasets.
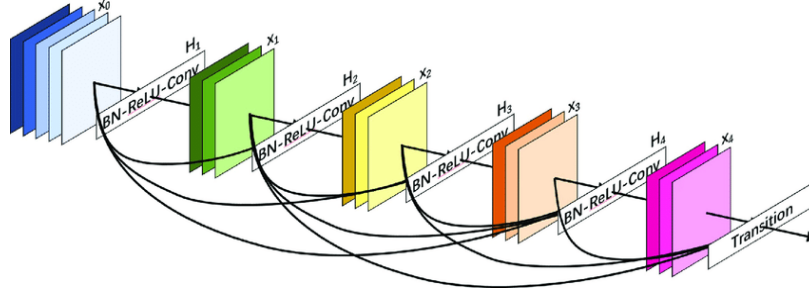

Fig 3: A Visual DenseNet Architecture Representation: A Simplified Overview

The DenseNet architecture consists of initial convolutional layers, followed by a sequence of densely connected convolutional layers (Dense blocks) interposed with several transition layers. It concludes with a Global Average Pooling (GAP) layer and a fully-connected layer (FC). In this design, the input RGB image with a height (H) and width (W) undergoes initial feature extraction via a Convolutional layer with 'k' filters. Each dense block concatenates feature maps—instead of summing them—to maintain constant dimensions for feature reuse and information flow.

This operation is viable through Batch normalization (BN) [29], Rectified Linear Unit (ReLU) activation [30], and a 3x3 Convolutional layer (Conv)—however, this concatenation increases the number of parameters in the network. To reduce dimensionality and control network growth, transition layers between the blocks use Batch Normalization, a 1x1 Conv layer, and a 2x2 average pooling layer. Finally, the GAP layer generates a single feature vector from the feature maps. This vector is fed into an FC layer with Softmax activation to produce the final output [31], [32]. Figure 2 above illustrates that the lth layer of the network concatenates the feature maps of preceding layers as a tensor $[x_0, x_1, ..., x_{l-1}]$, using the composite function H, mathematically represented as $x_l = H_l([x_0, x_1, ..., x_{l-1}])$.

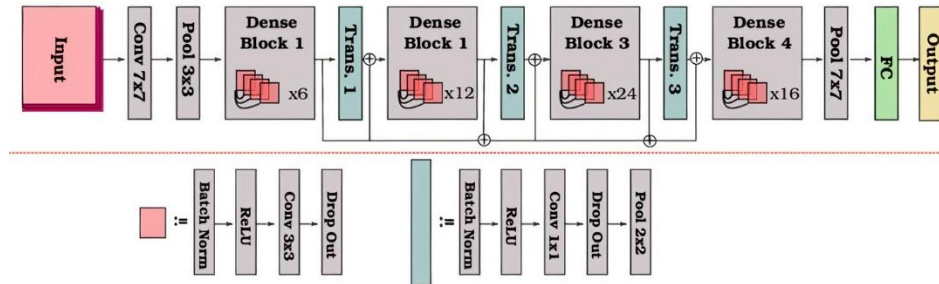**Fig 4:** An In-Depth Analysis of Blocks and Layers of DenseNet-121

This paper proposes the DenseNet-121 architecture for Chest X-ray image analysis. Compared to other DenseNet architectures, the design is preferred for medical image analysis due to its well-balanced, versatile, and lightweight architecture—making it easy to train, achieving high accuracy at high speed, and deploying on devices

with limited resources. DenseNet-121 architecture comprises 121 layers: (117) Convolutional layers, (3) pooling layers, and (1) Fully-connected layer. As indicated in Fig 4, It includes (4) dense blocks with a growth rate of 32, (3) transition layers, (1) global average pooling (GAP) layer, and (1) a fully connected layer. Since there are L (L+1)/2 direct connections for 'L' layers, DenseNet-121 architecture has 159 connections with more than 7 million learnable parameters—as interpreted in Table 1.

Table 1: A Summarized table comparing DenseNet-121 with other architecture from ImageNet

Layers	Output Size	DenseNet-121		DenseNet-169		DenseNet-201		DenseNet-264	
Convolution	112×112	7×7 conv, stride 2							
Pooling	56×56	3×3 max pool, stride 2							
Dense Block (1)	56×56	$\begin{bmatrix} 1 \times 1 \text{ conv} \\ 3 \times 3 \text{ conv} \end{bmatrix}$	$\times 6$	$\begin{bmatrix} 1 \times 1 \text{ conv} \\ 3 \times 3 \text{ conv} \end{bmatrix}$	$\times 6$	$\begin{bmatrix} 1 \times 1 \text{ conv} \\ 3 \times 3 \text{ conv} \end{bmatrix}$	$\times 6$	$\begin{bmatrix} 1 \times 1 \text{ conv} \\ 3 \times 3 \text{ conv} \end{bmatrix}$	$\times 6$
Transition Layer (1)	56×56	1×1 conv							
	28×28	2×2 average pool, stride 2							
Dense Block (2)	28×28	$\begin{bmatrix} 1 \times 1 \text{ conv} \\ 3 \times 3 \text{ conv} \end{bmatrix}$	$\times 12$	$\begin{bmatrix} 1 \times 1 \text{ conv} \\ 3 \times 3 \text{ conv} \end{bmatrix}$	$\times 12$	$\begin{bmatrix} 1 \times 1 \text{ conv} \\ 3 \times 3 \text{ conv} \end{bmatrix}$	$\times 12$	$\begin{bmatrix} 1 \times 1 \text{ conv} \\ 3 \times 3 \text{ conv} \end{bmatrix}$	$\times 12$
Transition Layer (2)	28×28	1×1 conv							
	14×14	2×2 average pool, stride 2							
Dense Block (3)	14×14	$\begin{bmatrix} 1 \times 1 \text{ conv} \\ 3 \times 3 \text{ conv} \end{bmatrix}$	$\times 24$	$\begin{bmatrix} 1 \times 1 \text{ conv} \\ 3 \times 3 \text{ conv} \end{bmatrix}$	$\times 32$	$\begin{bmatrix} 1 \times 1 \text{ conv} \\ 3 \times 3 \text{ conv} \end{bmatrix}$	$\times 48$	$\begin{bmatrix} 1 \times 1 \text{ conv} \\ 3 \times 3 \text{ conv} \end{bmatrix}$	$\times 64$
Transition Layer (3)	14×14	1×1 conv							
	7×7	2×2 average pool, stride 2							
Dense Block (4)	7×7	$\begin{bmatrix} 1 \times 1 \text{ conv} \\ 3 \times 3 \text{ conv} \end{bmatrix}$	$\times 16$	$\begin{bmatrix} 1 \times 1 \text{ conv} \\ 3 \times 3 \text{ conv} \end{bmatrix}$	$\times 32$	$\begin{bmatrix} 1 \times 1 \text{ conv} \\ 3 \times 3 \text{ conv} \end{bmatrix}$	$\times 32$	$\begin{bmatrix} 1 \times 1 \text{ conv} \\ 3 \times 3 \text{ conv} \end{bmatrix}$	$\times 48$
Classification Layer	1×1	7×7 global average pool							
		1000D fully-connected, softmax							

Model Design

Environmental Setup: The hardware utilized in this study includes an NVIDIA RTX 3070 GPU with CUDA support and 16 GB of RAM. The TensorFlow 2.11 framework is used with Python 3.9 in a Jupyter Notebook IDE, along with software libraries like NumPy, Pandas, Matplotlib, and ImageDataGenerator.

Training: The phase involved using the transfer learning to train preprocessed images with the DenseNet-121 architecture. Initially, the DenseNet was pre-trained as a feature extractor, and its fully connected layers were substituted with new classification layers—while freezing some initial layers. This approach allowed the model to utilize the knowledge acquired by DenseNet to perform classification, resulting in higher accuracy in a shorter period. The training process also employed a batch size of 64 and applied the ReLU activation function to all layers [33].

For the model's performance optimization, the training process minimized the binary cross-entropy loss using the Adam optimizer with a learning rate of 0.001 while avoiding overfitting on the validation set by employing early stopping with the patience of 5 epochs while training the model for 50 epochs [34].

- **ReLU (Rectified Linear Unit)**

$$f(z) = \max(0, z) \tag{1}$$

Where: z is the input to the activation function, max (0, z) returns the maximum value between 0 and z: simply returns the input value if it is positive, and 0 if it is negative.

- **Adam Optimizer**

$$m_t = \beta_{1}\, m_{t-1} + (1 - \beta_1)g_t \; , \; v_t = \beta_{1}\, v_{t-1} + (1 - \beta_1){g_t}^2$$

$$w_t = w_{t-1} - \alpha_i \frac{m\hat{}_t}{\sqrt{(v\hat{}_t + \varepsilon)}}, \; \text{where} \; m\hat{}_t = \frac{m_t}{(1-\beta_1^t)} \; and \; v\hat{}_t = \frac{v_t}{(1-\beta_2^t)} \tag{2}$$

Where α is a learning rate, m_t and v_t are the first and second moment estimate at time step 't' respectively, β is hyper parameter for controlling exponential decay rates as $\beta_1 = 0.9$ and $\beta_1 = 0.999$, and epsilon ($\varepsilon = 10^{-8}$).

- **Softmax Function**

$$\sigma(z\_i) = \frac{e^{z\_i}}{\sum_{j=1}^{k} e^{z\_j}} \tag{3}$$

Where z_i is the i-th input vector z, k is the number of classes in the multi-class classifier, e =e is the mathematical constant e $\approx$ 2.71828, and $\sum_{j=1}^{k} e^{z\_j}$ is the sum of the exponentiated values of all elements in the input vector z.

Table 2: A Model summary for pre-trained DenseNet-121 on a TensorFlow framework

```
Layer (type)                    Output Shape           Param #    Connected to
==================================================================================================
input_1 (InputLayer)            (None, None, None, 3    0

zero_padding2d_1 (ZeroPadding2D (None, None, None, 3    0          input_1[0][0]

conv1/conv (Conv2D)             (None, None, None, 6    9408       zero_padding2d_1[0][0]

conv1/bn (BatchNormalization)   (None, None, None, 6    256        conv1/conv[0][0]

conv1/relu (Activation)         (None, None, None, 6    0          conv1/bn[0][0]

zero_padding2d_2 (ZeroPadding2D (None, None, None, 6    0          conv1/relu[0][0]

pool1 (MaxPooling2D)            (None, None, None, 6    0          zero_padding2d_2[0][0]

conv2_block1_0_bn (BatchNormali (None, None, None, 6    256        pool1[0][0]

• • • •

conv5_block16_1_relu (Activatio (None, None, None, 1    0          conv5_block16_1_bn[0][0]

conv5_block16_2_conv (Conv2D)   (None, None, None, 3    36864      conv5_block16_1_relu[0][0]

conv5_block16_concat (Concatena (None, None, None, 1    0          conv5_block15_concat[0][0]
                                                                   conv5_block16_2_conv[0][0]

bn (BatchNormalization)         (None, None, None, 1    4096       conv5_block16_concat[0][0]

relu (Activation)               (None, None, None, 1    0          bn[0][0]
==================================================================================================
Total params: 7,037,504
Trainable params: 6,953,856
Non-trainable params: 83,648
```

Model Evaluation

The evaluation process utilized various metrics to assess the effectiveness of the designed model in analyzing test datasets. These metrics include Accuracy, Precision (PPV), Recall (Sensitivity), Specificity, Negative Predictive Value (NPV), and F1 score. However, due to the imbalanced dataset for classification tasks in the designed model, the AUC (Area under the Curve)-ROC (Receiver Operating Characteristic) was prioritized as the overall performance metric. [35].

AUC-ROC/ AUROC: The Area under the Receiver Operating Characteristics curve is a comprehensive and independent visualization metric that evaluates the performance of a model in classification problems. This metric considers both the True Positive Rate (Sensitivity/Recall) and False Positive Rate (Specificity), then provides a trade-off across a range of decision thresholds, thereby providing a single value that summarizes the model's performance and compares with the others. AUROC of 1 indicates that the model is excellent, while a value of 0 reflects a poor model, and 0.5 implies the model cannot distinguish between the classes.

Confusion Matrix
- **True positive (TP):** cases in which the model correctly predicted a positive outcome**.**
- **False positive (FP):** cases in which the model incorrectly predicted a positive outcome.
- **True negative (TN):** cases in which the model correctly predicted a negative outcome.
- **False negative (FN):** cases in which the model incorrectly predicted a negative outcome.

Evaluation Metrics Formulas

$$Accuracy = \frac{Number\ of\ Correct\ Predictions}{Total\ number\ of\ Predictions\ made} = \frac{TP+TN}{TP+TN+FP+FN} \tag{4}$$

$$Recall/TPR = \frac{Number\ of\ True\ Positive}{Total\ number\ of\ (actual)\ all\ Positive} = \frac{TP}{TP+FN} \tag{5}$$

$$Precision = \frac{Number\ of\ True\ Positive}{Total\ Positive\ Prediction} = \frac{TP}{TP+FP} \qquad (6)$$

$$F1\text{-}Score = \frac{2\ (precision\ x\ Recall)}{Precision+Recall} = \frac{2\ TP}{2TP+FP+FN} \qquad (7)$$

$$Specificity/FPR = \frac{Number\ of\ True\ (actual)\ Negative}{Total\ number\ of\ all\ Negative} = \frac{TN}{TN+FP} \qquad (8)$$

$$AUROC = \int_0^1 TPR(FPR)^{-1}\ dFPR \qquad (9)$$

III. Result

This section presents the findings of our study and addresses the research questions posed earlier. It discusses the evaluation metrics employed to assess the performance of a designed model and compares it with other state-of-the-art approaches reported in the literature.

Table 4: Comparison study between our designed model and among the best model in classifying Chest X-ray 14 Dataset using DenseNet-121 Architecture.

|	TP	TN	FP	FN	Accuracy	Sensitivity	Specificity	PPV	NPV	AUC	F1	TH
Cardiomegaly	16	814	169	1	0.83	0.941	0.828	0.086	0.999	0.963	0.158	0.5
Emphysema	20	869	103	8	0.899	0.714	0.894	0.163	0.991	0.965	0.256	0.5
Effusion	99	690	196	15	0.789	0.868	0.779	0.336	0.979	0.901	0.484	0.5
Hernia	1	743	255	1	0.754	0.5	0.774	0.004	0.999	0.712	0.008	0.5
Infiltration	114	543	256	78	0.697	0.594	0.672	0.302	0.874	0.726	0.399	0.5
Mass	40	789	158	13	0.829	0.755	0.833	0.202	0.984	0.888	0.319	0.5
Nodule	28	731	220	21	0.769	0.571	0.769	0.113	0.972	0.765	0.189	0.5
Atelectasis	64	657	249	30	0.791	0.681	0.725	0.204	0.956	0.781	0.314	0.5
Pneumothorax	24	785	183	8	0.809	0.75	0.811	0.116	0.99	0.826	0.201	0.5
Pleural_Thickening	24	713	259	4	0.757	0.857	0.734	0.085	0.994	0.868	0.154	0.5
Pneumonia	14	661	320	5	0.735	0.737	0.674	0.042	0.994	0.762	0.154	0.5
Fibrosis	10	725	261	4	0.755	0.714	0.735	0.037	0.995	0.801	0.07	0.5
Edema	15	767	213	5	0.782	0.75	0.789	0.066	0.994	0.856	0.121	0.5
Consolidation	36	658	297	9	0.698	0.8	0.689	0.108	0.987	0.812	0.19	0.5
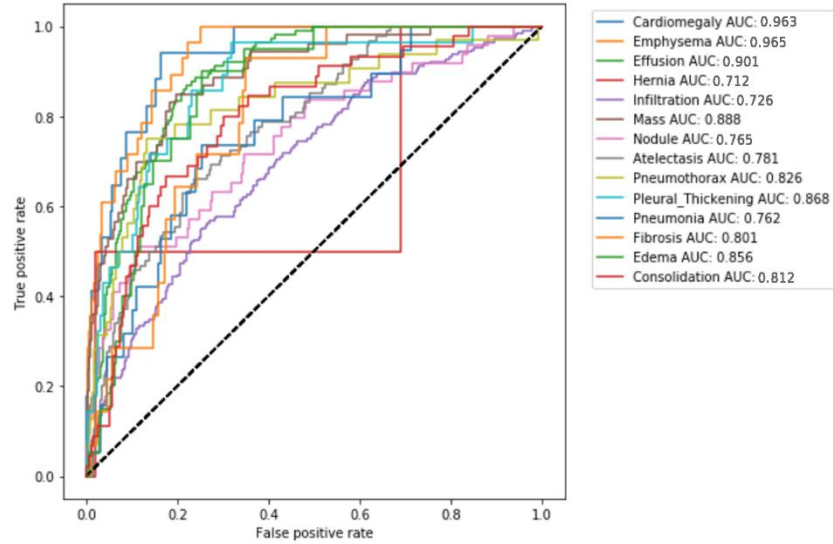
Fig 4: The Area under the ROC curve (AUROC) plotted with the Sensitivity (TPR of 1) against the Specificity (FPR of 0) at various Threshold settings (TH)—as presented in table 3.

Table 4: Comparison study between our designed model and among the best model in classifying Chest X-ray 14 Dataset using DenseNet-121 Architecture.

	Wang et al. (2017)	Yao et al. (2017)	CheXNet	Our Model
Emphysema	0.815	0.829	0.9371	0.965
Cardiomegaly	0.807	0.904	0.9248	0.963
Effusion	0.784	0.859	0.8638	0.901
Mass	0.706	0.792	0.8676	0.888
Pleural_Thickening	0.708	0.765	0.8062	0.868
Edema	0.835	0.882	0.8878	0.856
Pneumothorax	0.806	0.841	0.8887	0.826
Consolidation	0.708	0.788	0.7901	0.812
Fibrosis	0.769	0.767	0.8047	0.801
Atelectasis	0.716	0.772	0.8094	0.781
Nodule	0.671	0.717	0.7802	0.765
Pneumonia	0.633	0.713	0.7680	0.762
Infiltration	0.609	0.695	0.7345	0.726
Hernia	0.767	0.914	0.9164	0.712

IV. Discussion

The study evaluated the performance of the DenseNet-121 architecture in classifying lung diseases and abnormalities in chest X-ray images using the Chest X-ray 14 dataset. Through several evaluation metrics, the results show that the model achieved an overall NPV (97.9%), Specificity (0.765), Sensitivity (0.73), and Accuracy (77.8%)—a significant improvement over traditional machine learning with accuracy around 60-70%. The use of data augmentation, Adam optimization, and early stopping further enhanced the model's performance, making it superior to several other top-performing deep learning models—as indicated in Table 4 [24], [37], [38]. The model demonstrated superior classification accuracy for several diseases, including Emphysema, Cardiomegaly, Effusion, Mass, and Pleural_Thickening. It has also achieved an overall AUROC of 0.83, with a strong performance for Emphysema (0.965) and Cardiomegaly (0.963) while a relatively weaker performance for Infiltration (0.726) and hernia (0.712).

Limitation: Future research needs to address several limitations of this study, including the relatively small dataset and classes compared to other medical image datasets and poor image quality in some cases, such as blurry images, images with artifacts, or low contrast. The annotation of a dataset using natural language processing and expert radiologists may result in inconsistencies in image labeling. Furthermore, the variability of chest radiographs, such as patient demographics, imaging equipment, and technical factors like exposure settings and image resolution, can also impact the model's performance. Additionally, the Chest X-ray 14 dataset only contains images captured from a front-view perspective, which may limit the model's generalizability to other views.

Future work: The future research will focus on integrating the designed model into clinical practice and assess its performance in real-world settings—especially on mobile devices. However, several areas of improvement need to be addressed to enhance the model's performance based on the results and limitations of this study. These areas include increasing the dataset size, improving image quality, annotating datasets with more consistent labeling, expanding radiographs with different views, or developing more advanced deep-learning models. In addition, there is an opportunity to explore a multi-task learning approach to identify multiple abnormalities or diseases simultaneously and incorporate different model modalities, such as CT scans, to improve the accuracy and robustness of the chest X-ray analysis model.

V. Conclusion

In Summary, this study highlights that the developed deep learning-based CNN algorithm offers a promising solution to the challenges associated with the time-consuming and accurate interpretation of chest X-ray images. Such automated tools potentially improve patient outcomes, reduce healthcare costs, and ultimately save lives. Further research and development in this area will undoubtedly lead to even more sophisticated tools for medical image analysis, revolutionizing the field of radiology and enhancing the quality of healthcare globally. However, this model should not replace radiologists but rather than used as diagnostic support. Moreover, addressing privacy, security, and bias concerns is significant before extensively (large scale) deploying the model.

References

[1] A. Lorensia, R. V. Suryadinata, and I. N. Y. Diputra, "Risk Factors and Early Symptoms Related to Respiratory Disease in Pedicab Drivers in Surabaya," *KEMAS J. Kesehat. Masy.*, vol. 15, no. 2, Art. no. 2, 2019,. Available: http://repository.ubaya.ac.id/37026/

[2] P. Montnémery, P. Bengtsson, A. Elliot, L.-H. Lindholm, P. Nyberg, and C.-G. Löfdahl, "Prevalence of obstructive lung diseases and respiratory symptoms in relation to living environment and socio-economic group," *Respir. Med.*, vol. 95, no. 9, pp. 744–752, Sep. 2001, doi: 10.1053/rmed.2001.1129.

[3] GBD 2015 LRI Collaborators, "Estimates of the global, regional, and national morbidity, mortality, and aetiologies of lower respiratory tract infections in 195 countries: a systematic analysis for the Global Burden of Disease Study 2015," *Lancet Infect. Dis.*, vol. 17, no. 11, pp. 1133–1161, Nov. 2017, doi: 10.1016/S1473-3099(17)30396-1.

[4] "Prevalence and attributable health burden of chronic respiratory diseases, 1990–2017: a systematic analysis for the Global Burden of Disease Study 2017," *Lancet Respir. Med.*, vol. 8, no. 6, pp. 585–596, Jun. 2020, doi: 10.1016/S2213-2600(20)30105-3.

[5] H. Kilic *et al.*, "Effect of chronic lung diseases on mortality of prevariant COVID-19 pneumonia patients," *Front. Med.*, vol. 9, p. 957598, Oct. 2022, doi: 10.3389/fmed.2022.957598.

[6] S. J. Tzotzos, B. Fischer, H. Fischer, and M. Zeitlinger, "Incidence of ARDS and outcomes in hospitalized patients with COVID-19: a global literature survey," *Crit. Care Lond. Engl.*, vol. 24, no. 1, p. 516, Aug. 2020, doi: 10.1186/s13054-020-03240-7.

[7] D. C. Moncada, Z. V. Rueda, A. Macías, T. Suárez, H. Ortega, and L. A. Vélez, "Reading and interpretation of chest X-ray in adults with community-acquired pneumonia," *Braz. J. Infect. Dis. Off. Publ. Braz. Soc. Infect. Dis.*, vol. 15, no. 6, pp. 540–546, 2011.

[8] B. Moifo *et al.*, "Inter-Observer Variability in the Detection and Interpretation of Chest X-Ray Anomalies in Adults in an Endemic Tuberculosis Area," *Open J. Med. Imaging*, vol. 5, no. 3, Art. no. 3, Aug. 2015, doi: 10.4236/ojmi.2015.53018.

[9] R. M. Hopstaken, T. Witbraad, J. M. A. van Engelshoven, and G. J. Dinant, "Inter-observer variation in the interpretation of chest radiographs for pneumonia in community-acquired lower respiratory tract infections," *Clin. Radiol.*, vol. 59, no. 8, pp. 743–752, Aug. 2004, doi: 10.1016/j.crad.2004.01.011.

[10] S. Sakurada *et al.*, "Inter-rater agreement in the assessment of abnormal chest X-ray findings for tuberculosis between two Asian countries," *BMC Infect. Dis.*, vol. 12, p. 31, Feb. 2012, doi: 10.1186/1471-2334-12-31.

[11] "Artificial intelligence in healthcare: past, present and future - PubMed." https://pubmed.ncbi.nlm.nih.gov/29507784/ .

[12] K. G. van Leeuwen, M. de Rooij, S. Schalekamp, B. van Ginneken, and M. J. C. M. Rutten, "How does artificial intelligence in radiology improve efficiency and health outcomes?" *Pediatr. Radiol.*, vol. 52, no. 11, pp. 2087–2093, Oct. 2022,doi: 10.1007/s00247-021-05114-8.

[13] J. T. Wu *et al.*, "Comparison of Chest Radiograph Interpretations by Artificial Intelligence Algorithm vs Radiology Residents," *JAMA Netw. Open*, vol. 3, no. 10, p. e2022779, Oct. 2020, doi: 10.1001/jamanetworkopen.2020.22779.

[14] A. Yilmaz, A. A. Demircali, S. Kocaman, and H. Uvet, "Comparison of Deep Learning and Traditional Machine Learning Techniques for Classification of Pap Smear Images." arXiv, Sep. 11, 2020. Available: http://arxiv.org/abs/2009.06366

[15] Y. Lai, "A Comparison of Traditional Machine Learning and Deep Learning in Image Recognition," *J. Phys. Conf. Ser.*, vol. 1314, no. 1, p. 012148, Oct. 2019, doi: 10.1088/1742-6596/1314/1/012148.

[16] Y. LeCun, Y. Bengio, and G. Hinton, "Deep learning," *Nature*, vol. 521, no. 7553, Art. no. 7553, May 2015, doi: 10.1038/nature14539.

[17] "Deep Learning Techniques for Biomedical and Health Informatics | SpringerLink." https://link.springer.com/book/10.1007/978-3-030-33966-1

[18] A. Anaya-Isaza, L. Mera-Jiménez, and M. Zequera-Diaz, "An overview of deep learning in medical imaging," *Inform. Med. Unlocked*, vol. 26, p. 100723, Jan. 2021, doi: 10.1016/j.imu.2021.100723.

[19] E. Çallı, E. Sogancioglu, B. van Ginneken, K. G. van Leeuwen, and K. Murphy, "Deep learning for chest X-ray analysis: A survey," *Med. Image Anal.*, vol. 72, p. 102125, Aug. 2021, doi: 10.1016/j.media.2021.102125.

[20] X. Lessage, S. Mahmoudi, S. A. Mahmoudi, S. Laraba, O. Debauche, and M. A. Belarbi, "Chest X-ray Images Analysis with Deep Convolutional Neural Networks (CNN) for COVID-19 Detection," in *Healthcare Informatics for Fighting COVID-19 and Future Epidemics*, L. Garg, C. Chakraborty, S. Mahmoudi, and V. S. Sohmen, Eds., in EAI/Springer Innovations in Communication and Computing. Cham: Springer International Publishing, 2022, pp. 403–423. doi: 10.1007/978-3-030-72752-9_21.

[21] D. R. Sarvamangala and R. V. Kulkarni, "Convolutional neural networks in medical image understanding: a survey," *Evol. Intell.*, vol. 15, no. 1, pp. 1–22, 2022, doi: 10.1007/s12065-020-00540-3.

[22] R. Yamashita, M. Nishio, R. K. G. Do, and K. Togashi, "Convolutional neural networks: an overview and application in radiology," *Insights Imaging*, vol. 9, no. 4, pp. 611–629, Aug. 2018, doi: 10.1007/s13244-018-0639-9.

[23] K. Simonyan and A. Zisserman, "Very Deep Convolutional Networks for Large-Scale Image Recognition." arXiv, Apr. 10, 2015. doi: 10.48550/arXiv.1409.1556.

[24] X. Wang, Y. Peng, L. Lu, Z. Lu, M. Bagheri, and R. M. Summers, "ChestX-ray8: Hospital-scale Chest X-ray Database and Benchmarks on Weakly-Supervised Classification and Localization of Common Thorax Diseases," in *2017 IEEE Conference on Computer Vision and Pattern Recognition (CVPR)*, Jul. 2017, pp. 3462–3471. doi: 10.1109/CVPR.2017.369.

[25] A. Krizhevsky, I. Sutskever, and G. Hinton, "ImageNet Classification with Deep Convolutional Neural Networks," *Neural Inf. Process. Syst.*, vol. 25, Jan. 2012, doi: 10.1145/3065386.

[26] O. Russakovsky *et al.*, "ImageNet Large Scale Visual Recognition Challenge." arXiv, Jan. 29, 2015. doi: 10.48550/arXiv.1409.0575.

[27] Y. Xu and R. Goodacre, "On Splitting Training and Validation Set: A Comparative Study of Cross-Validation, Bootstrap and Systematic Sampling for Estimating the Generalization Performance of Supervised Learning," *J. Anal. Test.*, vol. 2, no. 3, pp. 249–262, Jul. 2018, doi: 10.1007/s41664-018-0068-2.

[28] G. Huang, Z. Liu, L. van der Maaten, and K. Q. Weinberger, "Densely Connected Convolutional Networks." arXiv, Jan. 28, 2018. doi: 10.48550/arXiv.1608.06993.

[29] S. Ioffe and C. Szegedy, "Batch Normalization: Accelerating Deep Network Training by Reducing Internal Covariate Shift." arXiv, Mar. 02, 2015. doi: 10.48550/arXiv.1502.03167.

[30] A. F. Agarap, "Deep Learning using Rectified Linear Units (ReLU)." arXiv, Feb. 07, 2019. doi: 10.48550/arXiv.1803.08375.

[31] X. Glorot, A. Bordes, and Y. Bengio, "Deep Sparse Rectifier Neural Networks," in *Proceedings of the Fourteenth International Conference on Artificial Intelligence and Statistics*, JMLR Workshop and Conference Proceedings, Jun. 2011, pp. 315–323. Accessed: Apr. 16, 2023. [Online]. Available: https://proceedings.mlr.press/v15/glorot11a.html

[32] R. Hu, B. Tian, S. Yin, and S. Wei, "Efficient Hardware Architecture of Softmax Layer in Deep Neural Network," in *2018 IEEE 23rd International Conference on Digital Signal Processing (DSP)*, Nov. 2018, pp. 1–5. doi: 10.1109/ICDSP.2018.8631588.

[33] S. J. Pan and Q. Yang, "A Survey on Transfer Learning," *IEEE Trans. Knowl. Data Eng.*, vol. 22, no. 10, pp. 1345–1359, Oct. 2010, doi: 10.1109/TKDE.2009.191.

[34] D. Shulman, "Optimization Methods in Deep Learning: A Comprehensive Overview." arXiv, Feb. 19, 2023. doi: 10.48550/arXiv.2302.09566.

[35] D. Powers, "Evaluation: From Precision, Recall and F-Factor to ROC, Informedness, Markedness & Correlation," *Mach Learn Technol*, vol. 2, Jan. 2008.

[36] A. C. J. W. Janssens and F. K. Martens, "Reflection on modern methods: Revisiting the area under the ROC Curve," *Int. J. Epidemiol.*, vol. 49, no. 4, pp. 1397–1403, Aug. 2020, doi: 10.1093/ije/dyz274.

[37] L. Yao, E. Poblenz, D. Dagunts, B. Covington, D. Bernard, and K. Lyman, "Learning to diagnose from scratch by exploiting dependencies among labels." arXiv, Feb. 01, 2018. doi: 10.48550/arXiv.1710.10501.

[38] P. Rajpurkar *et al.*, "CheXNet: Radiologist-Level Pneumonia Detection on Chest X-Rays with Deep Learning." arXiv, Dec. 25, 2017. Available: http://arxiv.org/abs/1711.05225